

# InverseMatrixVT3D: An Efficient Projection Matrix-Based Approach for 3D Occupancy Prediction

Zhenxing Ming, Julie Stephany Berrio, Mao Shan, and Stewart Worrall

**Abstract**— This paper introduces InverseMatrixVT3D, an efficient method for transforming multi-view image features into 3D feature volumes for 3D semantic occupancy prediction. Existing methods for constructing 3D volumes often rely on depth estimation, device-specific operators, or transformer queries, which hinders the widespread adoption of 3D occupancy models. In contrast, our approach leverages two projection matrices to store the static mapping relationships and matrix multiplications to efficiently generate global Bird’s Eye View (BEV) features and local 3D feature volumes. Specifically, we achieve this by performing matrix multiplications between multi-view image feature maps and two sparse projection matrices. We introduce a sparse matrix handling technique for the projection matrices to optimise GPU memory usage. Moreover, a global-local attention fusion module is proposed to integrate the global BEV features with the local 3D feature volumes to obtain the final 3D volume. We also employ a multi-scale supervision mechanism to further enhance performance. Comprehensive experiments on the nuScenes dataset demonstrate the simplicity and effectiveness of our method. The code will be made available at: <https://github.com/DanielMing123/InverseMatrixVT3D>

## I. INTRODUCTION

Understanding the surrounding scene’s three-dimensional (3D) geometry is fundamental to developing autonomous driving (AV) systems. While lidar-based methods [1]–[13] which utilize explicit depth measurements have been performing exceptionally well on public datasets [14]–[17], they are hindered by the expensive cost of sensors and the sparsity of data points. As a result, the broader application of lidar-based methods is limited.

In recent years, vision-centric AV systems have garnered significant attention as a promising strategy due to its cost-effectiveness, stability, and generality. By utilizing multi-camera images as inputs, this approach has demonstrated competitive performance across various 3D perception tasks, including depth estimation [18]–[20], 3D object detection [21]–[28], online high-definition (HD) map construction [29]–[33], and semantic map construction [34]–[36].

3D object detection based on fusing surround view cameras can play a crucial role in 3D perception. However, it faces challenges in handling new scenarios. One of the challenges is the finite number of semantic classes in the training dataset, making it difficult to create a model for every potential scenario that might be encountered on the road. In contrast, a more practical approach to depict the vehicle’s surrounding environment is by directly reconstructing the 3D scenes. In pursuit of this objective, several

This work has been supported by the Australian Centre for Robotics (ACFR). The authors are with the ACFR at the University of Sydney (NSW, Australia). E-mails: [zmin2675@uni.sydney.edu.au](mailto:zmin2675@uni.sydney.edu.au), [{j.berrio, m.shan, e.nebot, s.worrall}@acfr.usyd.edu.au](mailto:{j.berrio, m.shan, e.nebot, s.worrall}@acfr.usyd.edu.au)

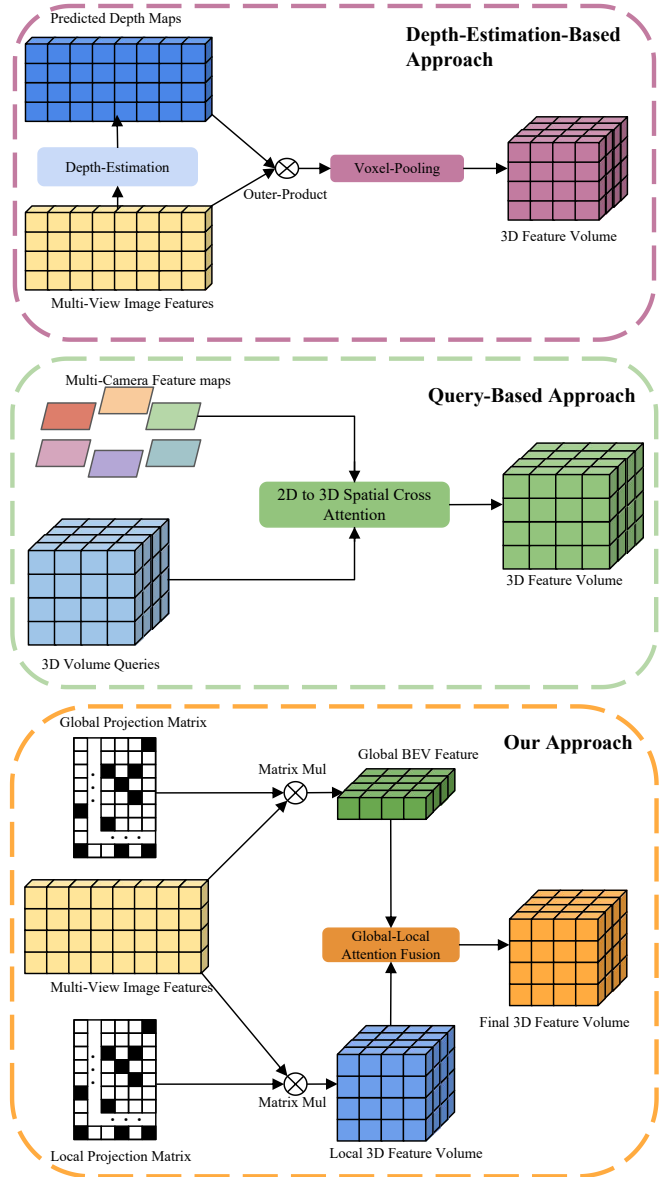


Fig. 1: The figure above shows the pipeline of three approaches: Depth-Estimation-based approach (upper), Query-based approach (middle), and our approach (lower). We simplify the generation of the 3D Feature Volume by adopting a matrix multiplication method.

methods [37]–[41] have been investigated to predict the 3D occupancy of a scene directly. These methods involve voxelizing the 3D space and assigning a probability to each voxel to determine its occupancy state—whether it is occupied or not. We argue that 3D occupancy serves as an adequate representation of the vehicle’s surrounding environment. This representation inherently ensures geometric consistency and can accurately describe occluded areas. Furthermore, it is more robust towards object classes that do not exist in the training dataset. Despite the promise of these methods, their inner structure is quite complex, and some methods require additional sensors to provide supervision signals. For instance, the method proposed in [40] relies on a lidar sensor to enhance performance through depth estimation supervision (Figure 1, upper). Additionally, the methods proposed in [38], [39] extensively employ query-based modules [42]–[44] to aggregate image features for the final 3D feature volume (Figure 1, middle).

To efficiently and effectively represent a 3D scene using 3D occupancy, we propose InverseMatrixVT3D (Figure 1, bottom). Our method focuses on constructing projection matrices and simplifying the generation of local 3D feature volumes and global Bird’s Eye View (BEV) features through matrix multiplication between multi-scale feature maps and projection matrices. Additionally, we employ a sparse matrix handling technique to optimize GPU memory usage when using these sparse projection matrices. Furthermore, we introduce a global-local fusion module to integrate global BEV features with local 3D feature volumes, resulting in the final 3D volume. We also apply a multi-scale supervision mechanism to each level to further enhance performance. Through comparisons with state-of-the-art (SOTA) algorithms on the nuScenes benchmark, we demonstrate our method’s simplicity and superior overall performance.

The main contributions of this paper are summarized below.

- The novel projection matrix-based approach is proposed to construct local 3D feature volumes and global BEV features.
- A global-local fusion module is proposed to integrate the information, resulting in the final 3D volume.
- We compare our approach with other state-of-the-art (SOTA) algorithms in the 3D semantic occupancy prediction task to prove the superior performance of our method.

The remainder of this paper is structured as follows: Section II provides an overview of related research and identifies the key differences between this study and previous publications. Section III outlines the general framework of InverseMatrixVT3D and offers a detailed explanation of the implementation of each module. Section IV presents the findings of our experiments. Finally, Section V provides the conclusion of our work.

## II. RELATED WORK

### A. Depth-Estimation-Based BEV Perception

Lift-Splat-Shoot (LSS) [21] introduced a lift operation for depth estimation using multi-view cameras. This process generates a pseudo-3D point cloud by merging the pseudo-3D points obtained from the multi-view images. The pseudo-3D point cloud is projected onto the ego vehicle coordinate system by leveraging intrinsic and extrinsic parameters. Subsequently, a splat operation is employed to accumulate features in the same BEV plane grid with varying z-direction heights, resulting in the final BEV features. This study pioneered the generation of BEV features through depth estimation and the fusion of multi-camera information in BEV perception. Another important contribution in this area was made by BEVDepth [24], highlighting the crucial impact of depth estimation precision on the model’s performance. To address this, BEVDepth introduced a real lidar-sensor based 3D point cloud as an additional supervision signal for the depth estimation stage. Furthermore, BEVStereo [25] improved depth estimation performance by introducing the temporal stereo method.

### B. Depth-Estimation Based 3D Semantic Occupancy Prediction

Based on the success of depth-estimation based BEV perception algorithms, several works [40], [41], [45], [46] have focused on constructing the 3D feature volume using pseudo-3D points. These approaches replace the previous splat operation, which generates the BEV feature, with a voxel-pooling operation. This new approach voxelizes the pseudo-3D point cloud and proposes several refinement modules to enhance the 3D feature volume. OCCFormer [40] introduces a dual-path transformer block to refine the BEV slice of the 3D feature volume, enhancing the long-range modelling capability of their model. FB-OCC [41] proposes an additional backward view-transformation module to improve the semantic information in the final 3D feature volume. Multi-Scale Occ [46] leverages a multi-scale fusion mechanism to capture global and local detail information in the 3D feature volume.

While depth-estimation-based approaches have achieved remarkable performance, they have one significant drawback: requiring depth ground truth labels to boost depth-estimation performance, which in turn boosts the model’s overall performance. This requirement introduces extra effort during the training process. In this paper, we propose a method that eliminates the need for depth estimation by solely relying on multi-view images to construct a 3D feature volume. Our approach achieves superior performance compared to depth-estimation based approaches.

### C. Query-Based BEV Perception

The BEVFormer series [26], [47] is one of the pioneering query-based approaches to BEV perception. By defining a BEV query plane and utilizing intrinsic and extrinsic parameters, the query vector in each grid of the BEV plane can be projected onto multi-view images, enabling the aggregation

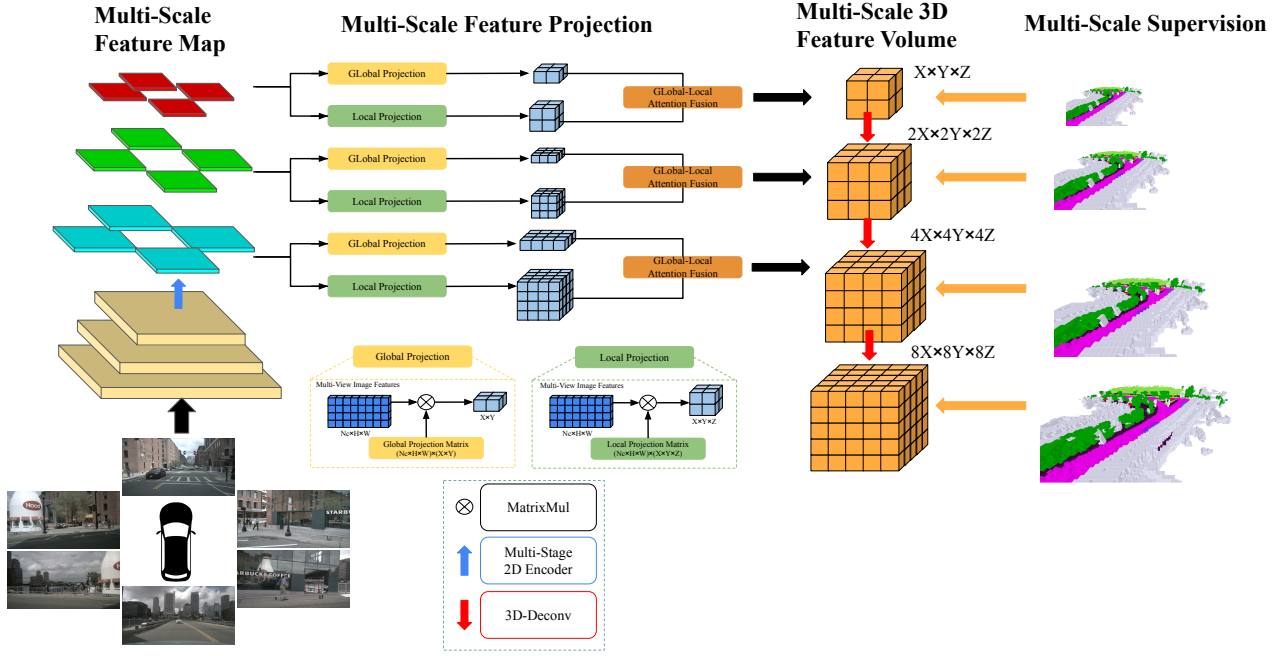


Fig. 2: **Overall architecture of InverseMatrixVT3D.** Firstly, the multi-camera images were inputted into the 2D backbone network to extract features at multiple scales. Subsequently, a multi-scale global local projection module was employed to construct multi-scale 3D feature volumes and BEV planes. A global-local attention fusion module was applied to each 3D feature volume and BEV plane at every level to obtain the final 3D feature volume. Finally, the 3D volume at each level was upsampled using 3D deconvolution for skip-connection, and a supervision signal was also applied at each level.

of features and the generation of the final BEV feature. The temporal self-attention module also leverages historical BEV features to enhance the model’s performance further. Similarly, the DETR3D [48] predefines a set of 3D query points as reference points. The intrinsic and extrinsic parameters are then used to project those points onto multi-view images to aggregate features. These works successfully eliminate the need for depth estimation by employing transformer blocks and relying solely on multi-view image features for BEV perception.

#### D. Query-Based 3D Semantic Occupancy Prediction

Building upon the success of query-based BEV perception algorithms, TPVFormer [38] introduces an extension to the BEV query by encompassing three perpendicular planes. This approach aims to capture the 3D world from multiple orthogonal perspectives. Similarly, SurroundOcc [39] further expands the three-perpendicular plane concept to a 3D query volume. Leveraging intrinsic and extrinsic parameters, each query vector is projected onto multi-view images to aggregate dense features. Additionally, PanoOcc [49] proposes an efficient method for processing the dense 3D feature volume using a sparse representation approach.

Given the success of query-based approaches, it is important to highlight that the extensive use of transformer blocks in these methods often results in slow and inefficient training processes and high GPU memory consumption. In contrast, our proposed method eliminates the requirement for transformer-based querying and depth estimation

while constructing the 3D feature volume. Our approach significantly improves model efficiency and enhances overall performance.

### III. INVERSEMATRIXVT3D

In this paper, our objective is to generate a dense 3D occupancy grid of the surrounding scene using multi-camera images  $Img = \{Img^1, Img^2, \dots, Img^N\}$ . Formally, the problem can be described as follows:

$$3DOcc = VT(Img^1, Img^2, \dots, Img^N) \quad (1)$$

where VT is the neural network that leverages the projection matrix to aggregate features for 3D occupancy, the final 3D occupancy prediction result denoted as  $3DOcc \in R^{X \times Y \times Z}$ , represents the semantic property of the grids and has values ranging from 0 to 16. In our case, a class value of 0 indicates that the grid is empty.

Figure 2 exhibits the overall architecture of our method. Initially, given a set of surrounding multi-camera images, we first use a 2D backbone network (e.g. ResNet101-DCN) to extract  $N_c$  cameras and  $L$  levels multi-scale features  $X = \left\{ \left\{ X_n^l \right\}_{n=1}^{N_c} \in R^{C_l \times H_l \times W_l} \right\}_{l=1}^L$ . For each level, we construct two projection matrices, namely, global projection matrix  $VT_{XY}^l \in R^{(N_c \times H_l \times W_l) \times (X_l \times Y_l)}$  and local projection matrix  $VT_{XYZ}^l \in R^{(N_c \times H_l \times W_l) \times (X_l \times Y_l \times Z_l)}$ . The feature maps at each level are multiplied with these projection matrices, resulting in the 3D feature volume  $F_{local}^l \in R^{C_l \times X_l \times Y_l \times Z_l}$  and the Bird’s-eye view (BEV)

feature  $F_{global}^l \in R^{C_l \times X_l \times Y_l}$ . Subsequently, the global-local attention fusion module merges information from these two features, producing the final 3D volume. Furthermore, the 3D volume at each level is upsampled using 3D deconvolution and integrated with the higher-level 3D volume through skip-connection. Finally, the dense occupancy ground truth from [39] is applied to supervise the 3D volume at each level with a decayed loss weight.

### A. Multi-Camera Images Feature Extractor

The purpose of the multi-camera image feature extractor is to capture both spatial and semantic features from the surrounding perspective view. These extracted features are the basis for the subsequent 3D occupancy prediction task. In our approach, we first employ a 2D backbone network to extract multi-scale feature maps. Then, a feature-pyramid network (FPN) is followed to further fuse feature output from different stages of the 2D backbone. The resulting feature maps have resolutions that are  $\frac{1}{8}$ ,  $\frac{1}{16}$ , and  $\frac{1}{32}$  of the input image resolution, respectively. The feature maps with smaller resolutions contain abundant semantic information, which assists the model in predicting the semantic class of each voxel grid. Conversely, the feature maps with larger resolutions provide richer spatial details and better guide the model regarding whether the current voxel grid is occupied or unoccupied.

### B. Global and Local Projection Matrix Generation

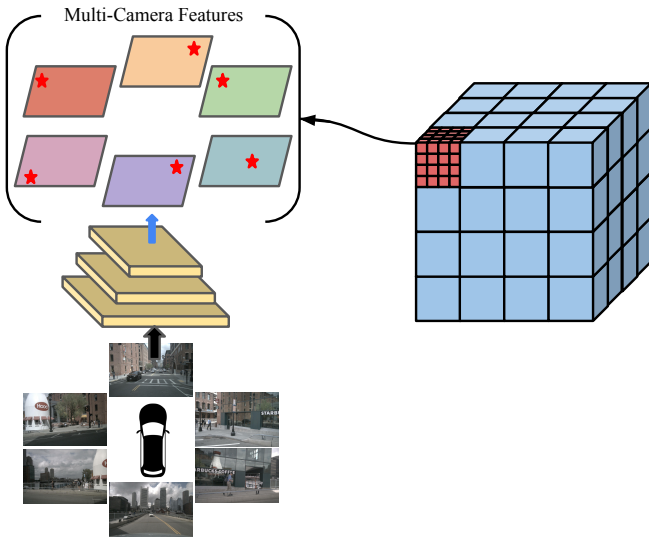


Fig. 3: The predefined 3D volume feature sampling process. Each voxel grid is initially divided into  $N^3$  subspaces along the vertical and horizontal directions, and the centre of each subspace serves as a sample point. These sample points are then projected onto all the multi-view feature maps to aggregate the corresponding features for the voxel grid.

In our approach, constructing global and local projection matrices is critical in gathering information for the local 3D feature volume and the global BEV feature. This differs from the method used in Occformer [40], which relies on

depth estimation and voxel pooling, or the methods employed in TPVFormer [38] and SurroundOcc [39], which involve transformer-based query. To begin with, we establish a set of predefined 3D volume spaces denoted by  $F_{3D}^l \in R^{X^l \times Y^l \times Z^l}$  for each level of multi-view feature maps under the ego vehicle’s coordinate system. The ego vehicle is positioned at the center of these 3D volumes. Within each 3D volume, we divide the voxel grid equally into  $N^3$  subspaces along the horizontal and vertical directions. Each center of the subspace serves as a sample point. Thus, for each level of the 3D volume space, we have a total of  $X^l \times Y^l \times Z^l \times N^3$  sample points. Next, we project each sample point from each voxel grid onto the corresponding level of multi-view feature map  $X^l$  using extrinsic and intrinsic parameters. Sample points that fall outside the boundaries of the feature maps or generate negative depth values are filtered out. The features hit by each sample point are then aggregated, resulting in a feature vector representing the corresponding voxel grid (see Figure 3).

The feature sampling process is a static mapping and can be represented by constructing the projection matrices  $VT\_XYZ^l \in R^{(N_c \times H_l \times W_l) \times (X_l \times Y_l \times Z_l)}$  as exhibited in Figure 4. Moreover, height information can be compressed further by constructing the projection matrix  $VT\_XY^l \in R^{(N_c \times H_l \times W_l) \times (X_l \times Y_l)}$  as shown in Figure 5. As a result, the generation of both the local 3D feature volume and global BEV feature can be greatly simplified as a matrix multiplication between the multi-view feature maps and the two projection matrices:

$$F_{local}^l = X^l \cdot VT\_XYZ^l \quad (2)$$

and

$$F_{global}^l = X^l \cdot VT\_XY^l \quad (3)$$

where  $X^l \in R^{N_c \times H_l \times W_l}$  represents the multi-view feature maps at the  $l$ -th level.

During the construction process of the global and local projection matrices, we observed that these matrices exhibit extensive sparsity. Consequently, the GPU memory utilization for constructing these matrices increases exponentially with their resolution. To optimize GPU memory utilization, we utilize the compressed sparse row (CSR) technique [50]. This technique stores only the non-zero values and their associated indices when constructing and storing the sparse matrices. By applying this technique, we can dramatically decrease the GPU memory usage for our highest 3D volume resolution from 15GB to 200MB.

### C. Global Local Attention Fusion

To enhance the ability of the final 3D feature volume to capture both global and local details, we introduce the Global-Local Attention Fusion module. The detailed structure of the Global-Local Attention Fusion module is depicted in Figure 6.

Inspired by [51], the module begins by applying traditional 2D and 3D convolution operations to enhance the global

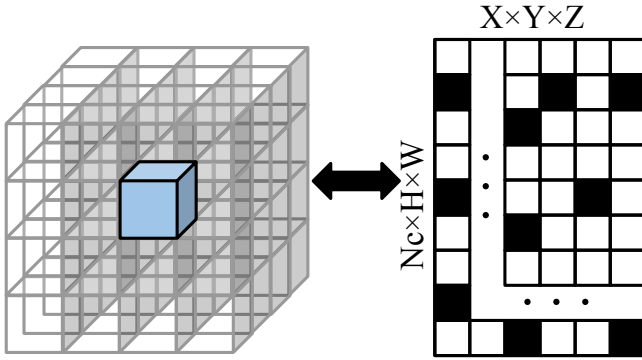


Fig. 4: The local projection matrix  $VT_{XYZ}$  represents the static mapping relationship for the feature sampling process of the local 3D feature volume.

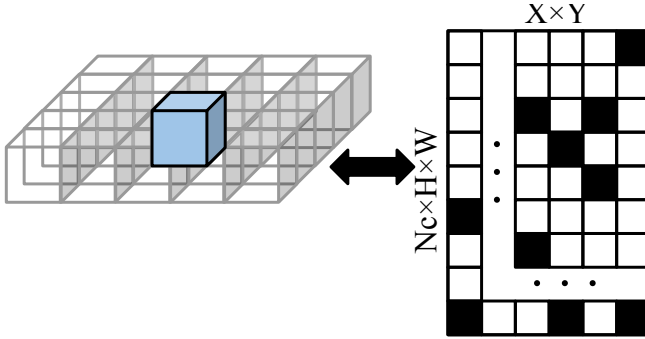


Fig. 5: The global projection matrix  $VT_{XY}$  represents the static mapping relationship for the feature sampling process of the global Bird’s Eye View (BEV) feature.

BEV feature and the local 3D feature volume. Building on recent advancements that emphasize the significance of locality and efficiency in transformers [52], [53] and the importance of the BEV plane [40], we incorporate an efficient window attention module from [52] and a bottleneck ASPP module to further refine the global BEV feature, enabling it to capture long-range global semantic information. Simultaneously, the local 3D feature volume is processed through the Feed-Forward Network (FFN) to generate attention weights. The BEV feature, refined by the window attention and bottleneck ASPP module, undergoes dimension expansion and is element-wise multiplied by the attention weights. This resulting feature is then added to the refined local 3D feature volume to produce the final 3D feature volume. The whole process can be described as follows:

$$F_{3DOcc}^l = F_{local}^l + \sigma(FNN(F_{local}^l)) \cdot Expand(F_{global}^l) \quad (4)$$

where  $\sigma(\cdot)$  refers to applying the sigmoid function to the output of the FFN; this function constrains the attention weight to the  $[0,1]$  range. Additionally, the Expand operation refers to expanding the dimension of  $F_{global}^l$  to match the dimension of  $F_{local}^l$ .

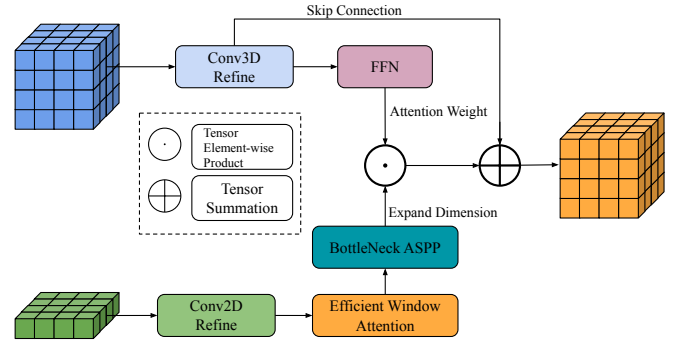


Fig. 6: The global-local fusion module. The global BEV feature and the local 3D feature volume are refined using traditional convolutional layers. The global BEV feature undergoes additional enhancement through an efficient window attention module and a bottleneck ASPP module. It then merges with the local 3D feature volume, resulting in the final 3D volume.

## IV. EXPERIMENTAL RESULTS

### A. Implementation Details

The  $InverseMatrixVT3D$  uses ResNet101-DCN [54], [55] as a 2D backbone with a checkpoint from FCOS3D [56] to extract image features. The features of stages 1,2,3 of the backbone are fed to FPN [57], resulting in 3-level multi-scale image features. The network architecture comprises four levels ( $L = 4$ ), with no skip connection applied to the highest level. For the paths corresponding to levels 1, 2, and 3, we employ divided schemas of  $N=3, 4,$  and  $5$ , respectively, to create sets of sample points. The AdamW optimizer with an initial learning rate of  $5e-5$  and weight decay of  $0.01$  is employed for optimization. The learning rate is decayed using a multi-step scheduler. For the 3D semantic occupancy prediction task, following the approach presented in [37], [39], we incorporate focal loss [58], Lovasz-softmax loss [59] and scene-class affinity loss [37] to handle the significant sparsity of free space in the ground truth dataset. Regarding data augmentation, random resize, rotation and flip operations are applied in the image space, following established practices for BEV-based 3D object detection [23]–[26] and the compared methods [37]–[40]. Our model includes two resolution settings. The predicted occupancy for evaluation is specified at a resolution of  $256 \times 256 \times 32$  and  $200 \times 200 \times 16$ , respectively. We further fixed the projection matrices under two resolution settings during testing to make the comparison. The model is trained using eight A10G GPUs with 24GB of memory, and it has been trained for 24 epochs on 3D semantic occupancy prediction tasks.

### B. Dataset

The nuScenes dataset [14], a vast autonomous driving dataset, serves as the data source for our experiments. As the test set lacks semantic labels, we train our model on the training set and assess its performance using the validation set. We set the range for occupancy prediction as  $[-50, 50]$  meters for the X and Y axes and  $[-5, 3]$  meters for

the Z axis. The input images have a  $1600 \times 900$  pixels resolution, while the final output occupancy is represented with a resolution of  $256 \times 256 \times 32$  for the base version and  $200 \times 200 \times 16$  for the small base version. We have conducted experiments on 3D semantic occupancy prediction tasks to provide quantitative results. The dense labels used for the 3D semantic occupancy prediction task are sourced from [39]. Additionally, we provide qualitative visualizations of the results for the 3D semantic occupancy prediction task.

### C. Performance Evaluate Metrics

To assess the performance of various state-of-the-art (SOTA) algorithms and compare them with our approach in the 3D semantic occupancy prediction task, we utilize the intersection over union (IoU) to evaluate each semantic class. Moreover, we employ the mean IoU overall semantic classes (mIoU) as a comprehensive evaluation metric:

$$IoU = \frac{TP}{TP + FP + FN} \quad (5)$$

and

$$mIoU = \frac{1}{Cls} \sum_{i=1}^{Cls} \frac{TP_i}{TP_i + FP_i + FN_i} \quad (6)$$

where  $TP$ ,  $FP$ , and  $FN$  represent the counts of true positives, false positives, and false negatives in our predictions, respectively, while  $Cls$  denotes the total class number.

### D. Model Performance Analysis

We perform the task of multi-camera 3D semantic occupancy prediction on the nuScenes dataset. To evaluate the performance of our proposed InverseMatrixVT3D, we compare it with SOTA algorithms and present the results in Table I. All methods are trained using dense 3D occupancy ground truth labels obtained from [39]. Our model has two different settings for two resolutions: the InverseMatrixVT3D(Base) and InverseMatrixVT3D(Small Base), which includes the projection matrices generation process, and the InverseMatrixVT3D(Fix) and InverseMatrixVT3D(Small Fix), which fixes the projection matrices. Our model displays remarkable performance in both settings in predicting crucial dynamic objects on the road, including buses, cars, construction vehicles, and trucks. Additionally, our model excels in identifying diverse background objects, such as drivable surfaces, terrain, and vegetation. These results unequivocally highlight our model’s superior 3D world modelling capability compared to other SOTA algorithms.

Our model aggregates features for the final 3D volume based on sampling at specific sampling locations. Compared to the transformer-based approach, whose sampling locations can be adjusted based on the query vector, our approach’s sampling locations are fixed. Thus, when dealing with some small objects such as traffic cones and bicycles, our method aggregates fewer features from the image and is inferior to SurroundOcc in predicting those classes. However, our sampling density is significantly larger than the transformer-based approach, enabling our method to make good predictions on relatively large objects in the scene. In summary, our

method sacrifices sampling flexibility to improve the sampling density. This underlying principle adjustment boosts model performance significantly in predicting relatively large objects in the scene.

### E. Challenging Scenes Qualitative Analysis

Figure 7a presents a scene where multiple objects of different semantic classes overlap and crowd. Despite this complexity, our method accurately predicts each object’s semantic class and 3D spatial location. Furthermore, the edges between objects of different classes are delineated. Figure 7b exhibits the scene where a construction vehicle is severely obscured by a large truck while multiple traffic cones and barriers crowd and overlap. Even under such a complex scenario, our model can still infer the general occupancy status of the construction vehicle and generate a meticulous 3D occupancy prediction with distinct boundaries.

We further demonstrate our model’s powerful 3D modelling capability by presenting the prediction results in challenging rainy and night-time scenes, as shown in Figure 8. In each subfigure, the prediction result generated by our model is displayed on the bottom left, while the ground truth is shown on the bottom right. Regarding the rainy scenario depicted in Figure 8a, we observed an inconsistency in the ground truth labels. This discrepancy is attributed to the lidar’s poor performance during rainy weather due to the reflection effect. Consequently, the ground truth labels become inconsistent. However, our model’s prediction result is remarkably accurate. It not only fills in the missing information from the ground truth but also successfully detects a pedestrian crossing the road (indicated by the red circle), even though the person is located at a significant distance from the ego vehicle. Moreover, in the night-time scene illustrated in Figure 8b, our model effectively predicts the presence of a motorcycle (marked by the red circle) in the distance ahead despite the low ambient light conditions.

We also present scenes showcasing crowded multiple objects and rainy day crossroads in Figure 9. The left column displays the multi-camera images, the middle column shows the prediction results of our model, and the right column exhibits the ground truth labels. In the scenarios with crowded multiple objects represented in the first and second rows of Figure 9, our model accurately segments each object. Furthermore, in the rainy city intersection scenario depicted in the last row of Figure 9, our model successfully predicts the road structure even in the presence of missing information in the ground truth labels.

### F. Model Efficiency

Table II presents a comparison of the inference time and inference memory among different methods. The experiments are conducted on a single RTX 3090 using six multi-camera images. All methods adopt an image resolution of  $1600 \times 900$ . The two base version models, which include the generation of projection matrices, have runtimes of 0.68 and 0.5 seconds for a single data sample. However, by fixing the projection matrices and removing the generation

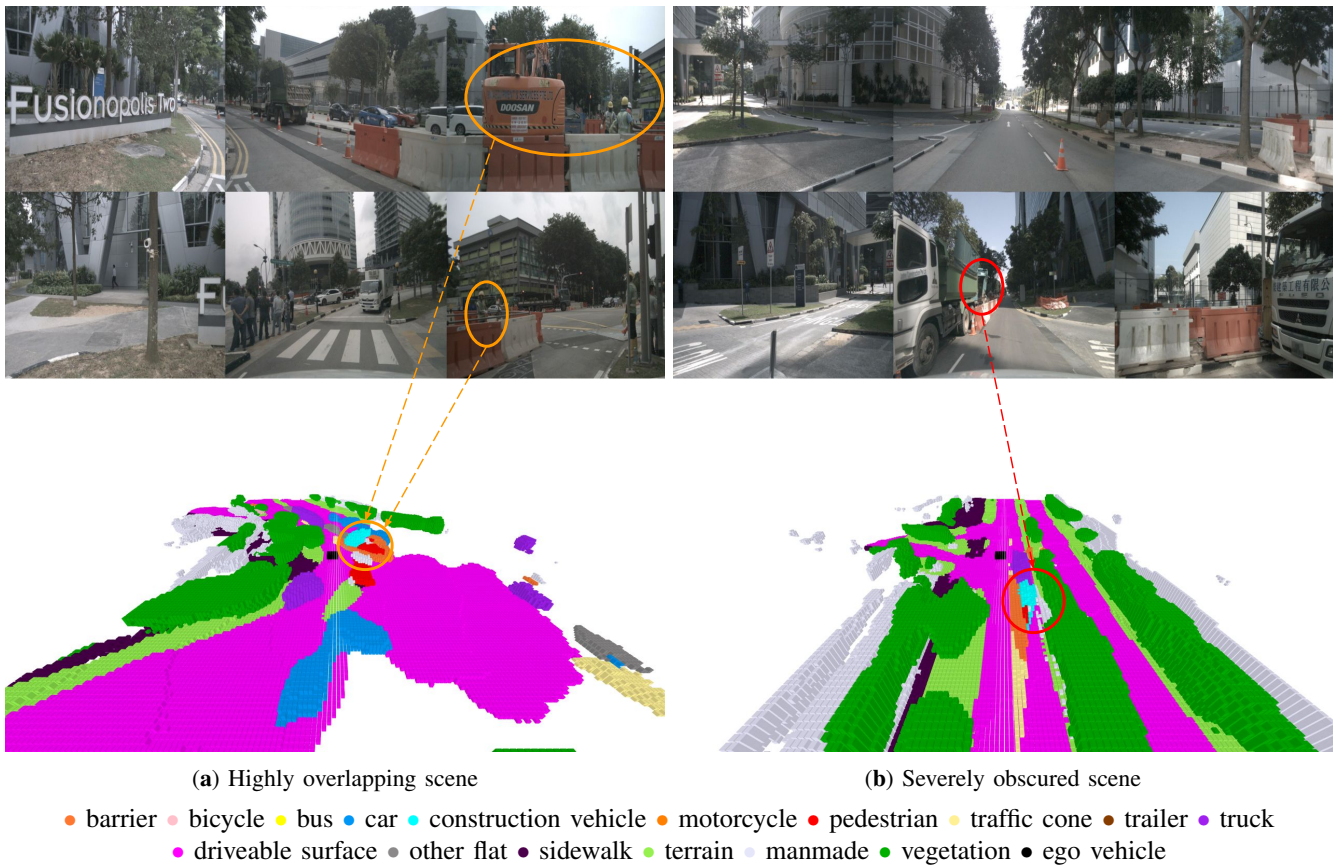


Fig. 7: Challenging scenes qualitative analysis. Despite the presence of multiple objects that overlap or severely obscure each other, our method is capable of accurately predicting detailed occupancy and delineating their edges. **Better viewed when zoomed in.**

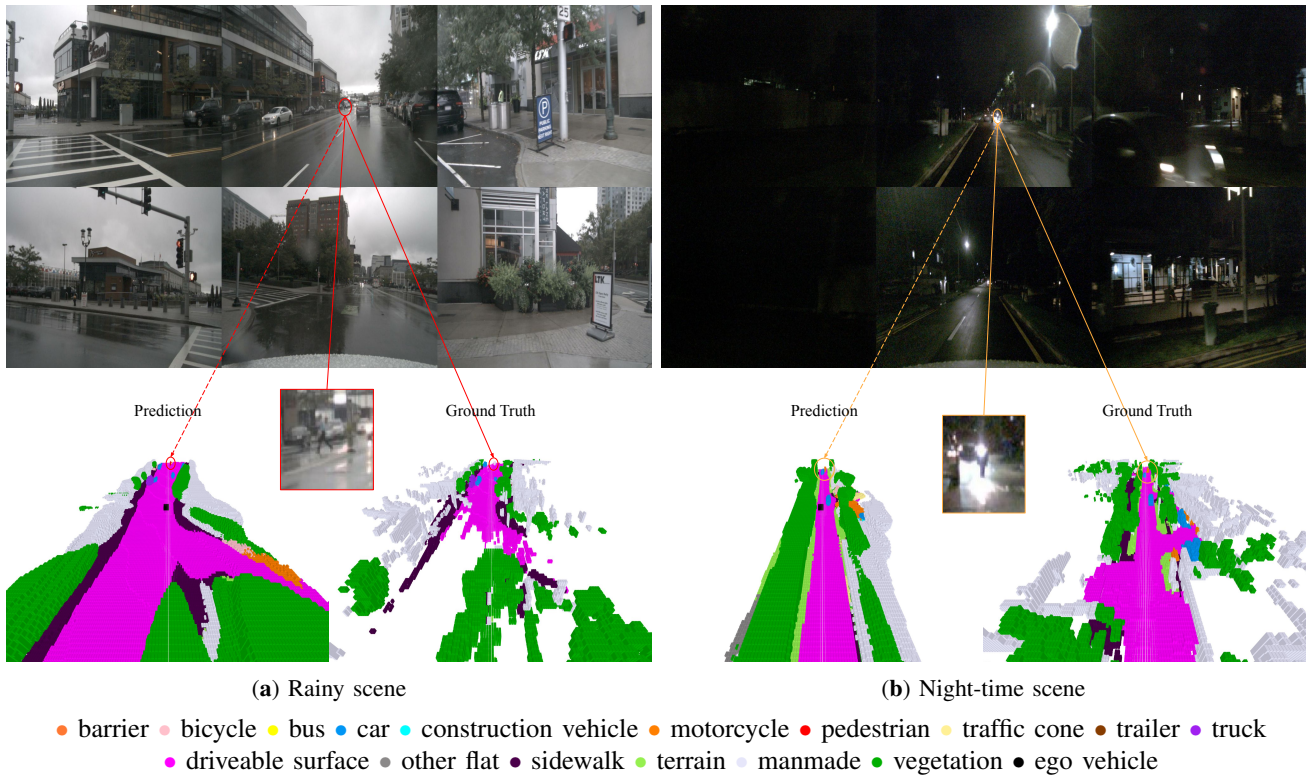


Fig. 8: Rainy and night-time scene. Despite challenging lighting conditions, our approach successfully predicts moving objects with high accuracy, even when they are far away from the ego vehicle. **Better viewed when zoomed in.**

Method	Resolution	3DOcc mIoU	barrier	bicycle	bus	car	const. veh.	motorcycle	pedestrian	traffic cone	trailer	truck	drive. surf.	other flat	sidewalk	terrain	manmade	vegetation
MonoScene [37]	200 × 200 × 16	7.31	4.03	0.35	8.00	8.04	2.90	0.28	1.16	0.67	4.01	4.35	27.72	5.20	15.13	11.29	9.03	14.86
Atlas [60]	200 × 200 × 16	15.00	10.64	5.68	19.66	24.94	8.90	8.84	6.47	3.28	10.42	16.21	34.86	15.46	21.89	20.95	11.21	20.54
BEVFormer [26]	200 × 200	16.75	14.22	6.58	23.46	28.28	8.66	10.77	6.64	4.05	11.20	17.78	37.28	18.00	22.88	22.17	13.80	22.21
TPVFormer [38]	200 × 200 × 16	17.10	15.96	5.31	23.86	27.32	9.79	8.74	7.09	5.20	10.97	19.22	38.87	21.25	24.26	23.15	11.73	20.81
SurroundOcc [39]	200 × 200 × 16	20.30	20.59	11.68	28.06	30.86	10.70	15.14	14.09	12.06	14.38	22.26	37.29	<b>23.70</b>	<b>24.49</b>	22.77	14.89	21.86
InverseMatrixVT3D (Base)	256 × 256 × 32	<b>26.03</b>	<b>26.15</b>	9.76	42.27	41.89	<b>17.83</b>	14.74	<b>22.88</b>	10.30	21.78	<b>36.90</b>	<b>50.82</b>	21.15	24.45	<b>26.76</b>	16.86	32.03
InverseMatrixVT3D (Small Base)	200 × 200 × 16	25.95	26.13	<b>15.19</b>	42.65	<b>43.92</b>	11.42	20.82	22.68	<b>13.45</b>	22.33	36.04	47.47	16.26	21.47	25.33	16.37	<b>33.73</b>
InverseMatrixVT3D (Fix)	256 × 256 × 32	24.58	23.19	7.86	<b>43.17</b>	43.16	16.80	16.03	18.16	8.81	<b>24.67</b>	35.93	41.60	17.68	21.11	21.54	<b>22.06</b>	31.45
InverseMatrixVT3D (Small Fix)	200 × 200 × 16	22.68	20.91	12.06	38.52	35.53	10.53	<b>21.49</b>	20.12	12.36	20.49	30.31	36.23	14.60	19.25	22.78	15.89	31.76

TABLE I: **3D semantic occupancy prediction results on nuScenes validation set.** All methods are trained with dense occupancy labels from [39].

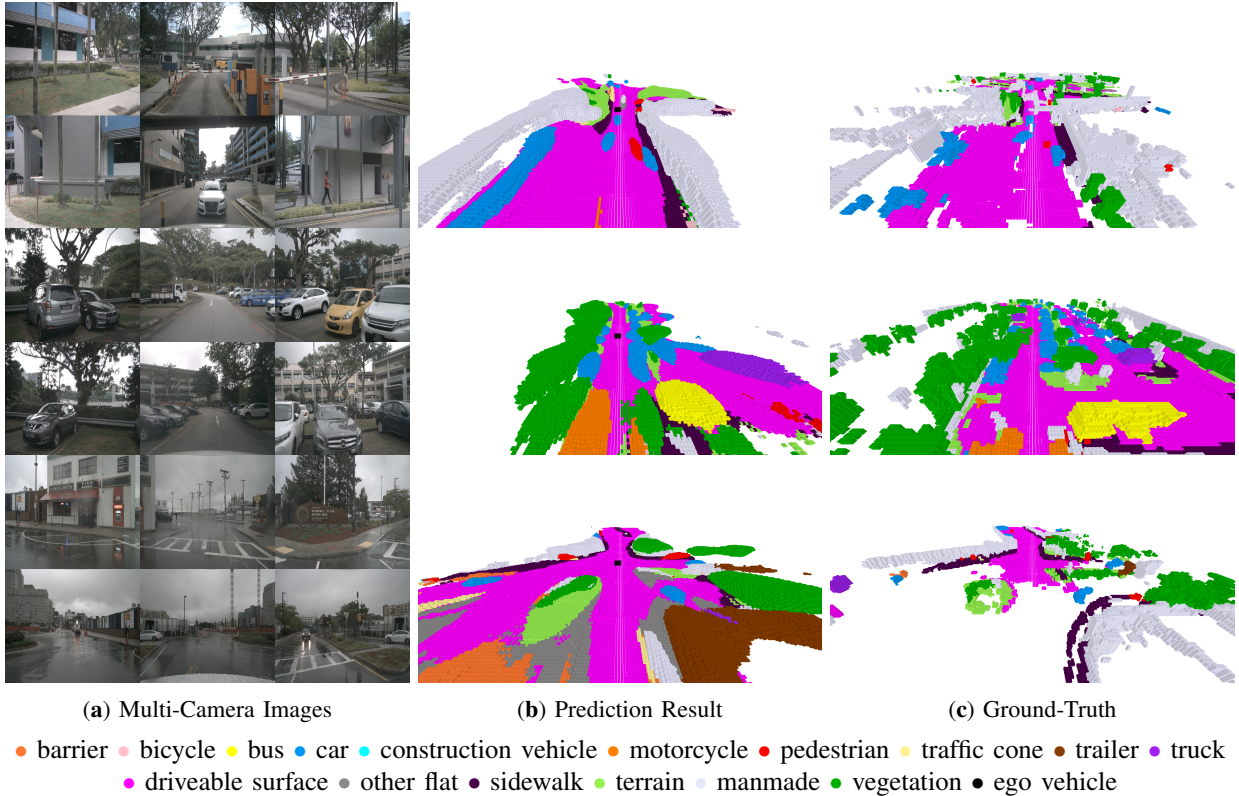


Fig. 9: Challenge scenes. Despite multiple different objects being crowded or missing information in the ground truth, our model can still accurately segment each object.

procedure, the fixed version model achieves exceptional real-time performance due to the utilization of projection matrices that facilitate 3D volume generation.

### G. Ablation Study

1) **Global Local Attention Fusion:** We perform an ablation study on the global-local attention fusion module, and the experiment results are presented in Table III. When we remove the fusion module and directly use the local 3D feature volume as the final 3D volume, we observe around 1.9% degradation in the model’s performance. This degradation could be attributed to the inability of the final 3D volume to capture long-range global semantic information.

2) **Multi-Scale Supervision:** We conducted an ablation study on the multi-scale supervision mechanism, and the experiment results are presented in Table IV. The upsample

and skip connection structure remains in the model where the multi-scale supervision mechanism is removed, but we only utilize the highest-level 3D feature volume for supervision. The experimental results demonstrate that the coarse-to-fine supervision schema can enhance performance by approximately 2.2%.

3) **Dividing Schemas For Each Level:** We performed an ablation study on the division schemas for each level, and the experiment results are presented in Table V. We used different N settings for levels 1, 2, and 3 to generate sample points, and the experimental results aligned with our expectations. Specifically, when the divide setting N is larger, more sample points can be generated, leading to dense sampling and rich feature aggregation. We also observed a trend where a larger divide setting at higher levels has a more significant impact on the final model performance, indicating

Method	Latency (s) (↓)	Memory (GB) (↓)
NeWCRFs [61]	1.07	14.5
MonoScene [37]	0.87	20.3
Adabins [62]	0.75	15.5
SurroundDepth [18]	0.73	12.4
SurroundOcc [39]	0.34	5.9
TPVFormer [38]	0.32	5.1
BEVFormer [26]	<b>0.31</b>	<b>4.5</b>
InverseMatrixVT3D (Base)	0.68	10.2
InverseMatrixVT3D (Small Base)	0.5	7.8
InverseMatrixVT3D (Fix)	0.45	4.88
InverseMatrixVT3D (Small Fix)	0.34	4.82

TABLE II: Model efficiency comparison of different methods. The experiments are performed on a single RTX 3090 using six multi-camera images. For input image resolution, all methods adopt  $1600 \times 900$ . ↓:the lower the better.

Method	3DOcc mIoU
w fusion module	<b>23.19</b>
w/o fusion module	21.32

TABLE III: Ablation study for global-local attention fusion module

the increased importance of higher-level feature aggregation.

## V. CONCLUSION

In this paper, we propose InverseMatrixVT3D, a method for vision-centric 3D semantic occupancy prediction. Our approach leverages predefined sample points for each scale of 3D volumes and constructs projection matrices to represent the fixed sampling process. Through matrix multiplication between multi-view feature maps and projection matrices in a multi-scale fashion, we generate local 3D feature volumes and global BEV features. These features are further merged using our proposed global-local fusion module, resulting in the final 3D volume at each level. Lastly, the 3D volumes at each level are upsampled and fused using a 3D deconvolution layer. Unlike other SOTA algorithms, our approach does not require depth estimation or transformer-based query, making the 3D volume generation process simple and efficient. Experimental results on nuScenes datasets demonstrate the superiority of our method in benchmark comparisons.

## REFERENCES

- [1] V. E. Liong, T. N. T. Nguyen, S. Widjaja, D. Sharma, and Z. J. Chong, "Amvnet: Assertion-based multi-view fusion network for lidar semantic segmentation," *arXiv preprint arXiv:2012.04934*, 2020.
- [2] A. H. Lang, S. Vora, H. Caesar, L. Zhou, J. Yang, and O. Beijbom, "Pointpillars: Fast encoders for object detection from point clouds," in *Proceedings of the IEEE/CVF conference on computer vision and pattern recognition*, 2019, pp. 12 697–12 705.
- [3] A. Milioto, I. Vizzo, J. Behley, and C. Stachniss, "Rangenet++: Fast and accurate lidar semantic segmentation," in *2019 IEEE/RSJ international conference on intelligent robots and systems (IROS)*. IEEE, 2019, pp. 4213–4220.
- [4] Y. Zhang, Z. Zhou, P. David, X. Yue, Z. Xi, B. Gong, and H. Foroosh, "Polarnet: An improved grid representation for online lidar point clouds semantic segmentation," in *Proceedings of the IEEE/CVF Conference on Computer Vision and Pattern Recognition*, 2020, pp. 9601–9610.

Method	3DOcc mIoU
w Multi-Scale Supervision	<b>23.19</b>
w/o Multi-Scale Supervision	21.07

TABLE IV: Ablation study for Multi-Scale Supervision

N setting of level 1,2,3	3DOcc mIoU
[3, 4, 5]	<b>23.19</b>
[2, 3, 4]	20.01
[1, 2, 3]	17.24
[1, 4, 6]	19.33

TABLE V: Ablation study of dividing schemas for each level

- [5] T. Cortinhal, G. Tzelepis, and E. Erdal Aksoy, "Salsanext: Fast, uncertainty-aware semantic segmentation of lidar point clouds," in *Advances in Visual Computing: 15th International Symposium, ISVC 2020, San Diego, CA, USA, October 5–7, 2020, Proceedings, Part II 15*. Springer, 2020, pp. 207–222.
- [6] H. Zhou, X. Zhu, X. Song, Y. Ma, Z. Wang, H. Li, and D. Lin, "Cylinder3d: An effective 3d framework for driving-scene lidar semantic segmentation," *arXiv preprint arXiv:2008.01550*, 2020.
- [7] X. Yan, J. Gao, J. Li, R. Zhang, Z. Li, R. Huang, and S. Cui, "Sparse single sweep lidar point cloud segmentation via learning contextual shape priors from scene completion," in *Proceedings of the AAAI Conference on Artificial Intelligence*, vol. 35, no. 4, 2021, pp. 3101–3109.
- [8] H. Tang, Z. Liu, S. Zhao, Y. Lin, J. Lin, H. Wang, and S. Han, "Searching efficient 3d architectures with sparse point-voxel convolution," in *European conference on computer vision*. Springer, 2020, pp. 685–702.
- [9] D. Ye, Z. Zhou, W. Chen, Y. Xie, Y. Wang, P. Wang, and H. Foroosh, "Lidarmultinet: Towards a unified multi-task network for lidar perception," in *Proceedings of the AAAI Conference on Artificial Intelligence*, vol. 37, no. 3, 2023, pp. 3231–3240.
- [10] M. Ye, R. Wan, S. Xu, T. Cao, and Q. Chen, "Drinet++: Efficient voxel-as-point point cloud segmentation," *arXiv preprint arXiv:2111.08318*, 2021.
- [11] R. Cheng, R. Razani, E. Taghavi, E. Li, and B. Liu, "2-s3net: Attentive feature fusion with adaptive feature selection for sparse semantic segmentation network," in *Proceedings of the IEEE/CVF conference on computer vision and pattern recognition*, 2021, pp. 12 547–12 556.
- [12] Q. Chen, S. Vora, and O. Beijbom, "Polarstream: Streaming object detection and segmentation with polar pillars," *Advances in Neural Information Processing Systems*, vol. 34, pp. 26 871–26 883, 2021.
- [13] S. Li, X. Chen, Y. Liu, D. Dai, C. Stachniss, and J. Gall, "Multi-scale interaction for real-time lidar data segmentation on an embedded platform," *IEEE Robotics and Automation Letters*, vol. 7, no. 2, pp. 738–745, 2021.
- [14] H. Caesar, V. Bankiti, A. H. Lang, S. Vora, V. E. Liong, Q. Xu, A. Krishnan, Y. Pan, G. Baldan, and O. Beijbom, "nuscnets: A multimodal dataset for autonomous driving," in *Proceedings of the IEEE/CVF conference on computer vision and pattern recognition*, 2020, pp. 11 621–11 631.
- [15] A. Geiger, P. Lenz, and R. Urtasun, "Are we ready for autonomous driving? the kitti vision benchmark suite," in *2012 IEEE conference on computer vision and pattern recognition*. IEEE, 2012, pp. 3354–3361.
- [16] J. Behley, M. Garbade, A. Milioto, J. Quenzel, S. Behnke, C. Stachniss, and J. Gall, "Semantickitti: A dataset for semantic scene understanding of lidar sequences," in *Proceedings of the IEEE/CVF international conference on computer vision*, 2019, pp. 9297–9307.
- [17] P. Sun, H. Kretzschmar, X. Dotiwalla, A. Chouard, V. Patnaik, P. Tsui, J. Guo, Y. Zhou, Y. Chai, B. Caine *et al.*, "Scalability in perception for autonomous driving: Waymo open dataset," in *Proceedings of the IEEE/CVF conference on computer vision and pattern recognition*, 2020, pp. 2446–2454.
- [18] Y. Wei, L. Zhao, W. Zheng, Z. Zhu, Y. Rao, G. Huang, J. Lu,

- and J. Zhou, "Surrounddepth: Entangling surrounding views for self-supervised multi-camera depth estimation," in *Conference on Robot Learning*. PMLR, 2023, pp. 539–549.
- [19] V. Guizilini, I. Vasiljevic, R. Ambrus, G. Shakhnarovich, and A. Gaidon, "Full surround monodepth from multiple cameras," *IEEE Robotics and Automation Letters*, vol. 7, no. 2, pp. 5397–5404, 2022.
- [20] A. Schmied, T. Fischer, M. Danelljan, M. Pollefeys, and F. Yu, "R3d3: Dense 3d reconstruction of dynamic scenes from multiple cameras," in *Proceedings of the IEEE/CVF International Conference on Computer Vision*, 2023, pp. 3216–3226.
- [21] J. Phillion and S. Fidler, "Lift, splat, shoot: Encoding images from arbitrary camera rigs by implicitly unprojecting to 3d," in *Computer Vision—ECCV 2020: 16th European Conference, Glasgow, UK, August 23–28, 2020, Proceedings, Part XIV 16*. Springer, 2020, pp. 194–210.
- [22] H. Zhou, Z. Ge, Z. Li, and X. Zhang, "Matrixvt: Efficient multi-camera to bev transformation for 3d perception," in *Proceedings of the IEEE/CVF International Conference on Computer Vision*, 2023, pp. 8548–8557.
- [23] J. Huang, G. Huang, Z. Zhu, Y. Ye, and D. Du, "Bevdet: High-performance multi-camera 3d object detection in bird-eye-view," *arXiv preprint arXiv:2112.11790*, 2021.
- [24] Y. Li, Z. Ge, G. Yu, J. Yang, Z. Wang, Y. Shi, J. Sun, and Z. Li, "Bevdepth: Acquisition of reliable depth for multi-view 3d object detection," in *Proceedings of the AAAI Conference on Artificial Intelligence*, vol. 37, no. 2, 2023, pp. 1477–1485.
- [25] Y. Li, H. Bao, Z. Ge, J. Yang, J. Sun, and Z. Li, "Bevstereo: Enhancing depth estimation in multi-view 3d object detection with temporal stereo," in *Proceedings of the AAAI Conference on Artificial Intelligence*, vol. 37, no. 2, 2023, pp. 1486–1494.
- [26] Z. Li, W. Wang, H. Li, E. Xie, C. Sima, T. Lu, Y. Qiao, and J. Dai, "Bevformer: Learning bird's-eye-view representation from multi-camera images via spatiotemporal transformers," in *European conference on computer vision*. Springer, 2022, pp. 1–18.
- [27] Z. Liu, H. Tang, A. Amini, X. Yang, H. Mao, D. L. Rus, and S. Han, "Befusion: Multi-task multi-sensor fusion with unified bird's-eye view representation," in *2023 IEEE International Conference on Robotics and Automation (ICRA)*. IEEE, 2023, pp. 2774–2781.
- [28] Y. Liu, T. Wang, X. Zhang, and J. Sun, "Petr: Position embedding transformation for multi-view 3d object detection," in *European Conference on Computer Vision*. Springer, 2022, pp. 531–548.
- [29] B. Liao, S. Chen, X. Wang, T. Cheng, Q. Zhang, W. Liu, and C. Huang, "Maptr: Structured modeling and learning for online vectorized hd map construction," *arXiv preprint arXiv:2208.14437*, 2022.
- [30] B. Liao, S. Chen, Y. Zhang, B. Jiang, Q. Zhang, W. Liu, C. Huang, and X. Wang, "Maptrv2: An end-to-end framework for online vectorized hd map construction," *arXiv preprint arXiv:2308.05736*, 2023.
- [31] Q. Li, Y. Wang, Y. Wang, and H. Zhao, "Hdmapnet: An online hd map construction and evaluation framework," in *2022 International Conference on Robotics and Automation (ICRA)*. IEEE, 2022, pp. 4628–4634.
- [32] Y. Liu, T. Yuan, Y. Wang, Y. Wang, and H. Zhao, "Vectormapnet: End-to-end vectorized hd map learning," in *International Conference on Machine Learning*. PMLR, 2023, pp. 22 352–22 369.
- [33] Y. Hu, J. Yang, L. Chen, K. Li, C. Sima, X. Zhu, S. Chai, S. Du, T. Lin, W. Wang *et al.*, "Planning-oriented autonomous driving," in *Proceedings of the IEEE/CVF Conference on Computer Vision and Pattern Recognition*, 2023, pp. 17 853–17 862.
- [34] Y. Zhang, Z. Zhu, W. Zheng, J. Huang, G. Huang, J. Zhou, and J. Lu, "Beverse: Unified perception and prediction in birds-eye-view for vision-centric autonomous driving," *arXiv preprint arXiv:2205.09743*, 2022.
- [35] A. Hu, Z. Murez, N. Mohan, S. Dudas, J. Hawke, V. Badrinarayanan, R. Cipolla, and A. Kendall, "Fiery: Future instance prediction in bird's-eye view from surround monocular cameras," in *Proceedings of the IEEE/CVF International Conference on Computer Vision*, 2021, pp. 15 273–15 282.
- [36] A. K. Akan and F. Güneş, "Stretchbev: Stretching future instance prediction spatially and temporally," in *European Conference on Computer Vision*. Springer, 2022, pp. 444–460.
- [37] A.-Q. Cao and R. de Charette, "Monoscene: Monocular 3d semantic scene completion," in *Proceedings of the IEEE/CVF Conference on Computer Vision and Pattern Recognition*, 2022, pp. 3991–4001.
- [38] Y. Huang, W. Zheng, Y. Zhang, J. Zhou, and J. Lu, "Tri-perspective view for vision-based 3d semantic occupancy prediction," in *Proceedings of the IEEE/CVF Conference on Computer Vision and Pattern Recognition*, 2023, pp. 9223–9232.
- [39] Y. Wei, L. Zhao, W. Zheng, Z. Zhu, J. Zhou, and J. Lu, "Surroundocc: Multi-camera 3d occupancy prediction for autonomous driving," in *Proceedings of the IEEE/CVF International Conference on Computer Vision*, 2023, pp. 21 729–21 740.
- [40] Y. Zhang, Z. Zhu, and D. Du, "Occformer: Dual-path transformer for vision-based 3d semantic occupancy prediction," *arXiv preprint arXiv:2304.05316*, 2023.
- [41] Z. Li, Z. Yu, D. Austin, M. Fang, S. Lan, J. Kautz, and J. M. Alvarez, "Fb-occ: 3d occupancy prediction based on forward-backward view transformation," *arXiv preprint arXiv:2307.01492*, 2023.
- [42] A. Vaswani, N. Shazeer, N. Parmar, J. Uszkoreit, L. Jones, A. N. Gomez, Ł. Kaiser, and I. Polosukhin, "Attention is all you need," *Advances in neural information processing systems*, vol. 30, 2017.
- [43] X. Dai, Y. Chen, J. Yang, P. Zhang, L. Yuan, and L. Zhang, "Dynamic detr: End-to-end object detection with dynamic attention," in *Proceedings of the IEEE/CVF International Conference on Computer Vision*, 2021, pp. 2988–2997.
- [44] X. Zhu, W. Su, L. Lu, B. Li, X. Wang, and J. Dai, "Deformable detr: Deformable transformers for end-to-end object detection," *arXiv preprint arXiv:2010.04159*, 2020.
- [45] T. V. J.-H. K. Myeongjin and K. S. J. S.-G. Jeong, "Milo: Multi-task learning with localization ambiguity suppression for occupancy prediction cvpr 2023 occupancy challenge report," *arXiv:2306.11414*, 2023.
- [46] Y. Ding, L. Huang, and J. Zhong, "Multi-scale occ: 4th place solution for cvpr 2023 3d occupancy prediction challenge," *arXiv preprint arXiv:2306.11414*, 2023.
- [47] C. Yang, Y. Chen, H. Tian, C. Tao, X. Zhu, Z. Zhang, G. Huang, H. Li, Y. Qiao, L. Lu *et al.*, "Befvformer v2: Adapting modern image backbones to bird's-eye-view recognition via perspective supervision," in *Proceedings of the IEEE/CVF Conference on Computer Vision and Pattern Recognition*, 2023, pp. 17 830–17 839.
- [48] Y. Wang, V. C. Guizilini, T. Zhang, Y. Wang, H. Zhao, and J. Solomon, "Detr3d: 3d object detection from multi-view images via 3d-to-2d queries," in *Conference on Robot Learning*. PMLR, 2022, pp. 180–191.
- [49] Y. Wang, Y. Chen, X. Liao, L. Fan, and Z. Zhang, "Panoocc: Unified occupancy representation for camera-based 3d panoptic segmentation," *arXiv preprint arXiv:2306.10013*, 2023.
- [50] A. Buluç, J. T. Fineman, M. Frigo, J. R. Gilbert, and C. E. Leiserson, "Parallel sparse matrix-vector and matrix-transpose-vector multiplication using compressed sparse blocks," in *Proceedings of the twenty-first annual symposium on Parallelism in algorithms and architectures*, 2009, pp. 233–244.
- [51] J. Hu, L. Shen, and G. Sun, "Squeeze-and-excitation networks," in *Proceedings of the IEEE conference on computer vision and pattern recognition*, 2018, pp. 7132–7141.
- [52] X. Liu, H. Peng, N. Zheng, Y. Yang, H. Hu, and Y. Yuan, "Efficientvit: Memory efficient vision transformer with cascaded group attention," in *Proceedings of the IEEE/CVF Conference on Computer Vision and Pattern Recognition*, 2023, pp. 14 420–14 430.
- [53] Z. Liu, Y. Lin, Y. Cao, H. Hu, Y. Wei, Z. Zhang, S. Lin, and B. Guo, "Swin transformer: Hierarchical vision transformer using shifted windows," in *Proceedings of the IEEE/CVF international conference on computer vision*, 2021, pp. 10 012–10 022.
- [54] K. He, X. Zhang, S. Ren, and J. Sun, "Deep residual learning for image recognition," in *Proceedings of the IEEE conference on computer vision and pattern recognition*, 2016, pp. 770–778.
- [55] J. Dai, H. Qi, Y. Xiong, Y. Li, G. Zhang, H. Hu, and Y. Wei, "Deformable convolutional networks," in *Proceedings of the IEEE international conference on computer vision*, 2017, pp. 764–773.
- [56] T. Wang, X. Zhu, J. Pang, and D. Lin, "Fcos3d: Fully convolutional one-stage monocular 3d object detection," in *Proceedings of the IEEE/CVF International Conference on Computer Vision*, 2021, pp. 913–922.
- [57] T.-Y. Lin, P. Dollár, R. Girshick, K. He, B. Hariharan, and S. Belongie, "Feature pyramid networks for object detection," in *Proceedings of the IEEE conference on computer vision and pattern recognition*, 2017, pp. 2117–2125.
- [58] T.-Y. Lin, P. Goyal, R. Girshick, K. He, and P. Dollár, "Focal loss for dense object detection," in *Proceedings of the IEEE international conference on computer vision*, 2017, pp. 2980–2988.

- [59] M. Berman, A. R. Triki, and M. B. Blaschko, “The lovász-softmax loss: A tractable surrogate for the optimization of the intersection-over-union measure in neural networks,” in *Proceedings of the IEEE conference on computer vision and pattern recognition*, 2018, pp. 4413–4421.
- [60] Z. Murez, T. Van As, J. Bartolozzi, A. Sinha, V. Badrinarayanan, and A. Rabinovich, “Atlas: End-to-end 3d scene reconstruction from posed images,” in *Computer Vision–ECCV 2020: 16th European Conference, Glasgow, UK, August 23–28, 2020, Proceedings, Part VII 16*. Springer, 2020, pp. 414–431.
- [61] W. Yuan, X. Gu, Z. Dai, S. Zhu, and P. Tan, “New crfs: Neural window fully-connected crfs for monocular depth estimation,” *arXiv preprint arXiv:2203.01502*, 2022.
- [62] S. F. Bhat, I. Alhashim, and P. Wonka, “Adabins: Depth estimation using adaptive bins,” in *Proceedings of the IEEE/CVF Conference on Computer Vision and Pattern Recognition*, 2021, pp. 4009–4018.